

3 November 2025

CO₂ Electroreduction on Borated Copper Surfaces: Boron Active Sites, not Copper

Anubhav Goswami¹, Zisheng Zhang^{1,2,3}, Anastassia Alexandrova¹

1. University of California, Los Angeles

2. Stanford University

3. SLAC National Accelerator Laboratory

Abstract

Boron-doped copper has recently emerged as an active and stable catalyst for the electrochemical reduction of CO₂ to value-added C₂ products. Here, we develop a realistic model of CO electroreduction on surface borides of copper under operational conditions, taking into account the effects of electrode potential, electrolyte environment, and pH. We study the possible reconstruction of the electrocatalyst surface using grand canonical DFT and global optimization to obtain a potential-dependent grand canonical ensemble description of metastable, hydrogen-covered catalyst surfaces. Two key surface configurations, low H-coverage (LC, -0.6 VSHE) and high H-coverage (HC, -0.8 VSHE) dominate this ensemble, with the former being kinetically persistent and C₂ selective under strongly reducing conditions. Nonmetallic boron sites on the surface copper boride are found to bind CO more strongly than copper sites, and mechanistic investigation of CO electroreduction pathways presents a surprisingly unconventional case of boron-centered reactivity in contrast to typical copper-centered reactivity. Neighboring boron sites present along boron chains on the surface copper boride are found to facilitate C–C coupling, thereby driving the high C₂ selectivity of this electrocatalyst.

Keywords

CO₂ Reduction Reaction, Boride, Grand canonical ensemble, Global optimization, Electrocatalysis, Electrochemical Interface, Surface Reconstruction, Kinetic Trapping

CO₂ Electroreduction on Borated Copper Surfaces: Boron Active Sites, not Copper

Anubhav Goswami,¹ Zisheng Zhang,^{1,3} Anastassia N. Alexandrova,^{1,2,*}

¹Department of Chemistry and Biochemistry, ²Department of Materials Science and Engineering, University of California, Los Angeles, USA, 90095-1569

³SUNCAT Center for Interface Science and Catalysis, Department of Chemical Engineering, Stanford University, Stanford, California, USA

Corresponding Author's email: alexandrova@g.ucla.edu

Abstract

Boron-doped copper has recently emerged as an active and stable catalyst for the electrochemical reduction of CO₂ to value-added C₂ products. Here, we develop a realistic model of CO electroreduction on surface borides of copper under operational conditions, taking into account the effects of electrode potential, electrolyte environment, and pH. We study the possible reconstruction of the electrocatalyst surface using grand canonical DFT and global optimization to obtain a potential-dependent grand canonical ensemble description of metastable, hydrogen-covered catalyst surfaces. Two key surface configurations, low H-coverage (LC, -0.6 V_{SHE}) and high H-coverage (HC, -0.8 V_{SHE}) dominate this ensemble, with the former being kinetically persistent and C₂ selective under strongly reducing conditions. Nonmetallic boron sites on the surface copper boride are found to bind CO more strongly than copper sites, and mechanistic investigation of CO electroreduction pathways presents a surprisingly unconventional case of boron-centered reactivity in contrast to typical copper-centered reactivity. Neighboring boron sites present along boron chains on the surface copper boride are found to facilitate C–C coupling, thereby driving the high C₂ selectivity of this electrocatalyst.

Introduction

Electrocatalysis provides a sustainable platform for storage of renewable energy and the production of value-added chemicals.^{1–4} Electrochemical reduction of CO₂ (eCO₂RR) is of added interest due to its potential toward closing the carbon cycle.^{5,6} For eCO₂RR, Cu is the only transition metal to effectively convert CO₂ to valuable multi-carbon (C₂₊) products such as ethylene and ethanol.^{7,8} There have been multiple strategies to increase C₂ product selectivity and to tune the product distribution, including the design of multicomponent electrocatalysts by introducing metal hydroxides,^{9,10} functionalizing electrodes with organic molecules to stabilize reaction intermediates,^{11,12} and doping Cu with non-metals to promote Cu⁺ states shown to be active for the C₂ production.^{13–20} In particular, B-doped Cu has recently been shown by Sargent et al. to exhibit remarkable performance for the selective synthesis of C₂ products while remaining stable for prolonged durations.²¹ Modelling eCO₂RR on such surfaces has been performed in the past on a simplistic subsurface model, or embedded B-atoms on the Cu(100) or Cu(111) surfaces, without incorporating realistic reaction

conditions.^{21,22} However, an accurate description of the electrocatalyst surface and accounting for its possible restructuring under operating conditions, by taking into consideration effects such as electrode potential, presence of electrolyte, and solution pH, is necessary to develop an understanding of these catalysts and their performance.

Here, we model eCORR reactions under realistic operational conditions. The starting point is the previously experimentally characterized ordered surface borides of copper on Cu(111).^{23–25} We constructed potential-dependent grand canonical ensemble and free energy landscape of the copper boride surface, to identify relevant coverage of *H at neutral pH and varying cathodic potentials. Both thermodynamic and kinetic considerations (accounting for reconstruction, dissolution, and hydrogen evolution reaction) are made to produce the relevant surface models, and to identify routes to potential surface degradation. At relevant cathodic potentials, CO adsorption showed a strong preference for B sites over Cu sites. Surprisingly, further mechanistic investigations revealed that B sites generally outperform Cu sites in CORR and are particularly superior for C–C coupling, leading to C₂ products. This work presents an unconventional instance wherein CORR chemistry occurs almost exclusively on B sites rather than Cu sites in contrast to typical non-metal doped Cu, and provides insights to develop an understanding of the activity, selectivity, and stability of this surface in catalyzing eCO₂RR. This will allow for the development of superior heterogeneous electrocatalysts for the efficient conversion of CO₂ to multi-carbon products.

Results and Discussion

Modelling electrocatalyst surface

We considered the ordered copper boride (referred to as CuB hereon) surface with stoichiometry Cu₈B₁₄ which is reported to form after the deposition of boron on Cu(111) under ultrahigh vacuum. We constructed the unit cell consisting of a 4 × 1 supercell of CuB on a 3-layer $\sqrt{73} \times \sqrt{39}$ superstructure of Cu(111), as reported experimentally,²³ corresponding to a repeating Cu₃₂B₅₆ surface (Figure 1a). The pH, electric double layers, and electrode potential can cause substantial restructuring of the surface, and therefore, the configuration of the CuB surface under the coverage of H was subjected to global optimization using the grand canonical genetic algorithm (GCGA).^{26–29} Notably, we sampled the positions of the Cu and B, and coverage of H atoms, to pursue possible reconstruction. The system was allowed to exchange H with a reservoir of hydrogen atoms held at a fixed chemical potential μ_H defined as:

$$\mu_H(\text{pH}, U, T) = \frac{1}{2} E_{\text{H}_2}^{\text{gas}} - \ln(10) k_B T \text{pH} - |e| U_{\text{SHE}} + (ZPE^{\text{gas}} + C_p^{\text{gas}} - TS^{\text{gas}}) - (ZPE^{\text{ads}} + C_p^{\text{ads}} - TS^{\text{ads}})$$

GCGA searches were carried out at the pH of 7 and multiple electrode potentials between 0 and -1.50 V_{SHE} to minimize the coverage-dependent grand canonical free energy Ω_{ads} defined as:

$$\Omega_{\text{ads}} = U - TS - \mu_H N_H \approx E^{\text{slab}-n_H} - E^{\text{slab}} - n_H \mu_H$$

In total, 4,191 unique structures for the CuB surface under H coverage were obtained. The results of grand canonical sampling at four cathodic potentials (-0.25 V_{SHE}, -0.50 V_{SHE}, -0.75

V_{SHE} , and $-1.00 V_{\text{SHE}}$) are illustrated in Figure 1 with H coverage represented by $\theta_{\text{H}} = n_{\text{H}}/n_{\text{B}}$. At $-0.25 V_{\text{SHE}}$, the process of H uptake by the CuB surface is initially thermodynamically unfavorable until around $\theta_{\text{H}} = 1.0$, beyond which, further hydrogenation appears to be comparatively favorable but still overall endergonic. At more negative electrode potentials (Figure 1c-e), the H uptake becomes thermodynamically favorable compared to the bare surface without hydrogen. At $-0.5 V$ (Figure 1c), a plateau of metastability appears, corresponding to a set of deep hydrides of the CuB surface. The hydrogenation occurs on the surface boron, in contrast to pure Cu surfaces that uptake H at cathodic potentials.^{26–28} The preferential hydrogenation of B atoms over Cu atoms is likely due to stronger, covalent bonding in B–H compared to more ionic bonding in Cu–H. This is demonstrated by analyzing features of the charge density ρ using QTAIM (Quantum Theory of Atoms In Molecules).^{30,31} Higher values of ρ (>0.1 a.u.) and generally negative values of $\nabla^2\rho$ (i.e. the Laplacian) at the B–H bond critical points are indicative of their covalent nature while the contrastingly lower values of ρ (<0.09 a.u.) and positive values of $\nabla^2\rho$ indicate ionic bonding in the Cu–H bonds (Figure S14). The sampling also shows that the thermodynamic global optimum corresponds to the uptake of even more H, with gradual breaking off of B atoms as borane-like structures, leading finally to the destruction of the B chains and likely borane dissolution. Besides borane formation, no substantial change of zigzag boron structures occurs, despite the sampling algorithm permitting it. Given the experimentally seen stability of the boron dopants on Cu in electroreduction conditions,²¹ it appears that the degradation must be prevented by kinetic effects, i.e. substantial barriers to excess hydrogenation and/or B chain breaking (*vide infra*) and competing hydrogen evolution reaction (HER) which maintains intermediate H coverage on the surface. Indeed, under non-equilibrium conditions that persist in thermal and electrochemical conditions, it has been observed that relaxation of the system to the thermodynamic global minimum can exceed relevant reaction timescales.^{26,28,32} For example, H coverage on Cu electrodes has been previously shown to be substantially lower than the thermodynamic prediction.²⁸ Along similar lines, we conjecture that the surface is trapped on the metastable hydride plateau (outlined in Figure 1c) during CO_2RR . Therefore, we constrained the upper limit of H coverage to ensure that the system has a maximum of one break-off B unit. Here, we only focus on the metastable H coverage regime outlined in Figure 1c (corresponding to GCGA sampling conducted at $-0.5 V_{\text{SHE}}$) and shown explicitly in Figure 1f, i.e., where θ_{H} ranges from 0.45 to 0.90 (corresponding to $n_{\text{H}} = 25$ to 50 per unit cell). This region exhibits a convex hull structure (Figure 1f), indicative of a local optimum in coverage. Note that for every θ_{H} , multiple possible structures are in a low energy window. A sub-ensemble is therefore constructed with configurations within 0.2 eV (corresponding to an equivalent Boltzmann population cutoff of 0.0005) of the global minimum at each coverage from the pool of configurations obtained from the GCGA sampling conducted at $-0.5 V_{\text{SHE}}$. This sub-ensemble covers the range where the B chains are majorly preserved on the surface due to kinetics, and only a minor breakage is observed.

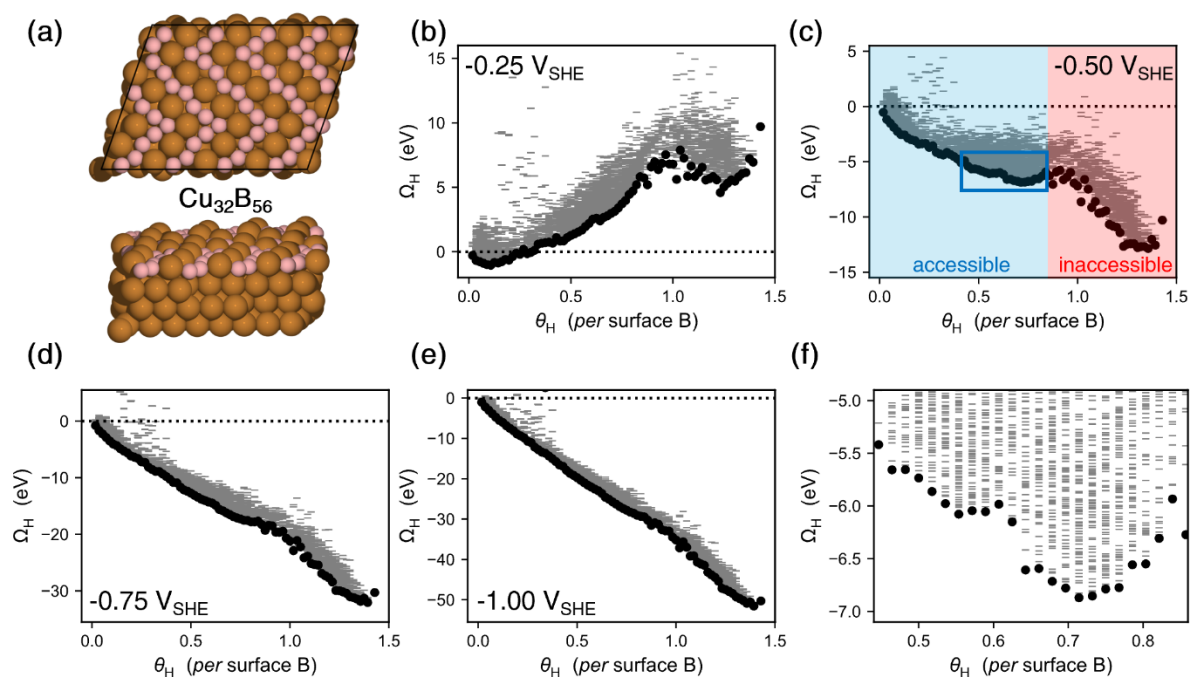


Figure 1. (a) $\text{Cu}_{32}\text{B}_{56}/\text{Cu}(111)$ unit cell. (b)–(e) Grand canonical free energy as a function of H coverage (in terms of θ_{H}), at different electrochemical potentials (vs SHE); each dash corresponds to a unique sampled local minimum with the global minimum at each H coverage marked with a circle. The region shaded blue indicates the upper limit of H coverage adopted in this work, beyond which, in the region shaded red, the system is considered losing boron to the solution phase. The plateau of metastability in (c) is indicated with a blue box. (f) The metastable region at $-0.5 \text{ V}_{\text{SHE}}$ as marked in (c); this convex hull is observed with a local optimum at $\theta_{\text{H}} = 0.7$.

To assess the evolution of the surface H coverage under varying electrochemical potentials, we computed potential-dependent free energies for the states within the sub-ensemble via GCDFT and calculated their populations using Boltzmann statistics in the relevant potential regime (Figure 2). In the window of -0.5 V to $-0.7 \text{ V}_{\text{SHE}}$, structures with lower H coverage ($\theta_{\text{H}} < 0.66$) and no B chain breaking dominate. Around the electrochemical potential of $-0.7 \text{ V}_{\text{SHE}}$, this preference switches to higher H coverage ($\theta_{\text{H}} > 0.66$) along with the initiation of B chain breaking. The configurations with higher H coverage include triply and quadruply hydrogenated B sites, with the latter being present as break-off units (Figure 2). However, B chain breaking associated with the excess hydrogenation of the B sites was found to have substantial kinetic barriers that are outcompeted by HER on these multiply hydrogenated B sites (see Supporting Information, Section S2), which likely prevents complete hydrogenation of the surface B atoms and subsequent dissolution, providing additional support for our prior assumption of kinetic metastability of the surface (*vide supra*). The sharp switch to higher H coverage (Figure 2) is also likely to be restrained by these kinetic barriers to B chain breaking and as such, we anticipate the lower H coverage structures to dominate the catalyst ensemble at operational timescales. The hydrogen-covered CuB surfaces were also found to be stable over 10 ps of unconstrained *ab initio* molecular dynamics (AIMD) simulations with explicit solvation, with no additional B chain breakage or B units floating into solution (see Supporting Information, Section S3). We found that within the region of potential importance in CO_2RR , i.e., -0.6 to $-0.9 \text{ V}_{\text{SHE}}$, the structures with $\theta_{\text{H}} = 0.46$ ($n_{\text{H}} = 26$ per unit cell) and $\theta_{\text{H}} = 0.70$ ($n_{\text{H}} = 39$ per unit cell) have a particularly high (sometimes exclusive) population. Additionally, a

single configuration corresponding to the global minimum (as shown in Figure 2) was found to contribute almost exclusively in case of both of the above coverages, i.e., for $\theta_H = 0.46$ near $-0.6 V_{SHE}$ and $\theta_H = 0.70$ near $-0.8 V_{SHE}$ (Figure S3). These configurations, hereafter referred to as low coverage, or LC ($-0.6 V_{SHE}$), and high-coverage, HC ($-0.8 V_{SHE}$), respectively (with the inclusion of the approximate potential at which each dominates the Boltzmann ensemble included in the nomenclature) were subjected to further investigation for their activity toward electrochemical CO reduction.

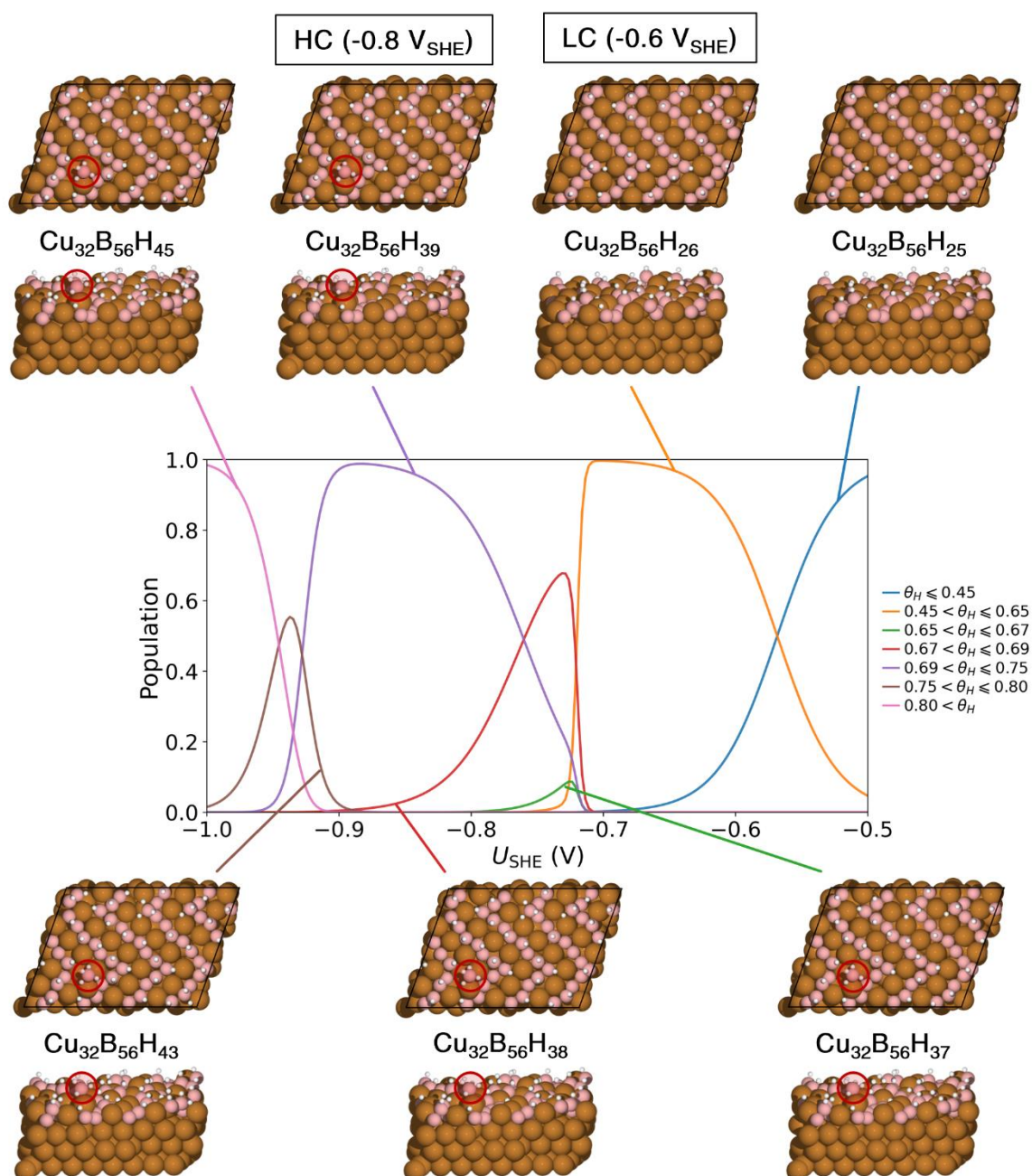


Figure 2. Boltzmann population of different H coverage ensembles as functions of electrochemical potential. The minimum energy structures (top and side views along with the stoichiometry of the corresponding unit cell) of each ensemble are shown, and break-off B units are circled in red. The predominant configurations LC ($-0.6 V_{SHE}$) and HC ($-0.8 V_{SHE}$) are denoted separately.

Bader charge analysis of the pristine and H-covered CuB (overall charge-neutral) surface was carried out to understand the influence of H coverage on the electronic structure of the surface (Figure 3). For the pristine surface, the surface B and Cu atoms carry an average Bader charge of $-0.24 e$ and $+0.29 e$ respectively, indicating oxidation of the surface Cu by the B atoms. Specifically, among the B atoms, those at the corners of the zigzag B chains are least negatively charged and become progressively more negatively charged toward the center of the zigzag chains.^{23,24} The B atoms covered with H atoms, having transferred electron density to the respective H atoms, are positively charged. Among the B atoms without B-H bonds, the extent of negative charge is seen to follow the geometric trend observed for the pristine surface. Therefore, the final charge of a surface B atom depends on both the presence or absence of H atoms bound to it and its location in the B chain, i.e., a combination of charge transfer to and from coordinating H and Cu atoms on the surface.

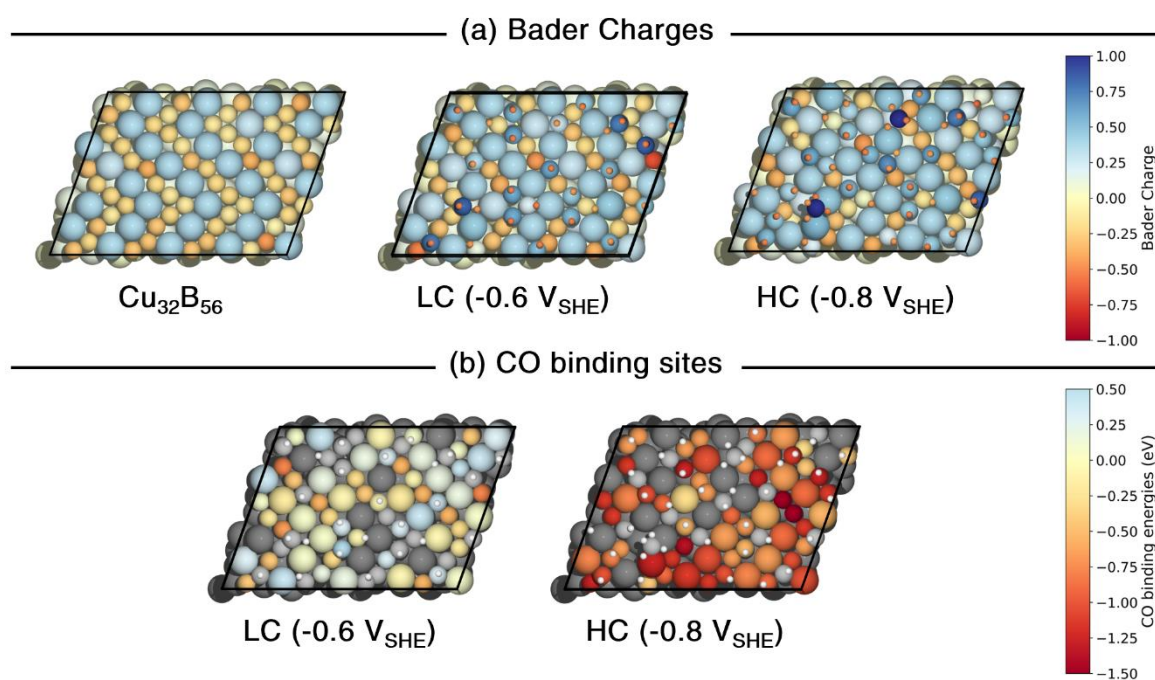


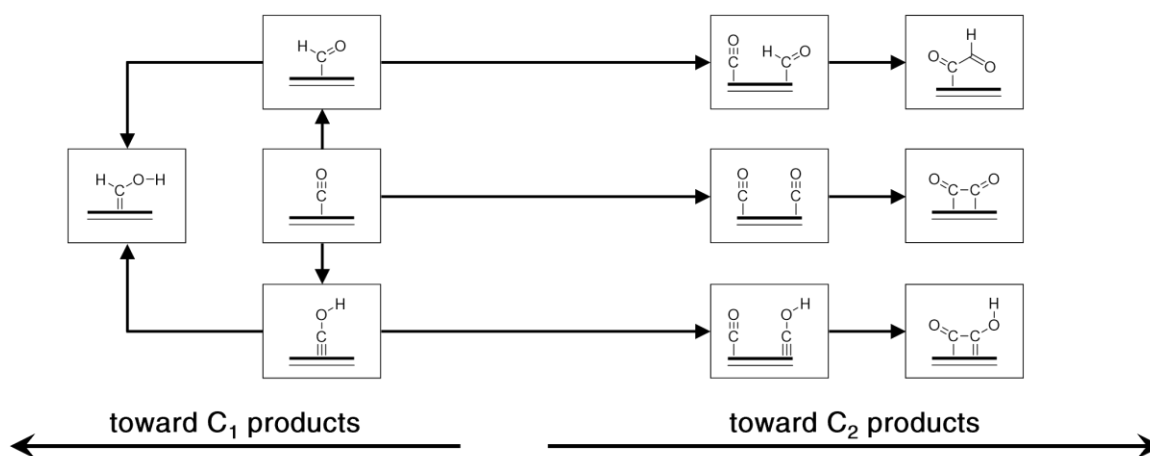
Figure 3. (a) Bader charges of the pristine and H-covered CuB surface configurations LC ($-0.6 V_{\text{SHE}}$) and HC ($-0.8 V_{\text{SHE}}$) which dominate the Boltzmann ensemble at $-0.6 V_{\text{SHE}}$ and $-0.8 V_{\text{SHE}}$ respectively. (b) Site-dependent CO binding energies on the predominant H-covered CuB surface configurations. Note that sites where CO did not bind successfully are colored dark grey and light grey for Cu and B respectively.

To identify potential sites for CORR, we sampled CO binding at different sites on the hydrogenated CuB surface. The large size of the unit cell made an extensive GCGA sampling of CO (in addition to surface restructuring and H coverage) prohibitively expensive, and we therefore resorted to a combination of one-shot sampling methods implemented in GOCIA²⁹ for CO adsorption (see Supporting Information, Note 2). The CO binding sites thus obtained are visualized in Figure 3b with their associated binding energies. The strongest CO binding corresponds to a binding energy ($\Delta E_{\text{b,CO}}$) of $-0.76 eV$ (corresponding binding free energy,

$\Delta G_{b,CO} = -0.22$ eV) at LC (-0.6 V_{SHE}) and -1.49 eV ($\Delta G_{b,CO} = -0.82$ eV) at HC (-0.8 V_{SHE}). It was observed that, in general, CO preferentially binds to the B atoms rather than the Cu atoms on the surface at both LC (-0.6 V_{SHE}) and HC (-0.8 V_{SHE}). We attribute this to the higher electron density on the B atoms relative to Cu, which leads to enhanced electrostatic attraction for the protons arriving from solution, and stronger boron-to-ligand π -backbonding, therefore strengthening the B-CO bond compared to the Cu-CO bond (see Supporting Information, Section S5). In some cases, CO binds to H-covered B sites by displacing the adsorbed *H to a neighboring site; however, these instances do not correspond to the strongest CO binding (Figure 3b). Most of the other B sites capable of binding CO strongly generally fall into one of two categories, being part of either a B₃₊ chain, i.e., three or more consecutive B atoms without H atoms, or part of a B₂ chain, i.e., two consecutive B atoms without H atoms. This categorization is anticipated to be useful later in the context of C₂ reaction pathways since C-C coupling on B sites in a B₂ chain necessitates CO adsorption on neighboring B atoms whereas on B sites in a B₃₊ chain, it may proceed from CO adsorption on alternate B atoms. We consider a number of these CO binding sites (both B and Cu) for subsequent mechanistic investigation at each of the above electrochemical conditions.

Mechanistic study of C₁ and C₂ pathways

Achieving a high C₂ vs C₁ selectivity during eCORR is of fundamentally high importance, and B-doped Cu has been reported to be highly selective for the formation of C₂ products.²¹ To this end, we carried out mechanistic studies of C₁ and C₂ pathways on the CuB surface under applied electrochemical potential and the appropriate surface H coverage. Previous mechanistic studies modelling CO reduction on Cu have identified key steps and intermediates leading ultimately to C₁ and C₂ products (Scheme 1).^{33–37} For C₁ products, this involves the hydrogenation of CO to CHO or COH and their subsequent hydrogenation to CHOH, which ultimately leads to C₁ products. For C₂ products, the reaction proceeds via the C-C coupling of neighboring CO molecules to produce CO-CO, or of CO with a hydrogenated intermediate to produce CO-COH or CO-CHO. These are the reaction intermediates we modelled on the different B and Cu sites as discussed above.



Scheme 1. CORR pathways toward C₁ and C₂ products.

The reaction intermediates for the C₁ and C₂ pathways were modelled on various CO binding sites at LC (-0.6 V_{SHE}) and HC (-0.8 V_{SHE}) (Figure 4). To keep the problem tractable, we used a ΔG_{b,CO} cutoff of 0.6 eV (compared to the strongest CO binding site) when considering various sites for this mechanistic investigation. This results in 20 and 22 different sites respectively in the two electrochemical conditions, as highlighted in Figure 4a,d. At LC (-0.6 V_{SHE}), all the sites satisfying this cutoff at B sites and we therefore took the strongest CO binding Cu site (marked as site 4 in Figure 4a) additionally into consideration, to be comprehensive. For each reaction intermediate, a spectrum of site-dependent free energies is observed, of which, the site corresponding to the minimum free energy is highlighted and numbered in Figure 4a,d.

The ensemble-averaged reaction free energy for each process, ⟨ΔG_{rxn}⟩, is thus obtained by Boltzmann-weighting the ΔG_{rxn} values, using ΔG_{b,CO} at that site as a weighting factor:

$$\langle \Delta G_{\text{rxn}} \rangle = \frac{\sum_i \Delta G_{\text{rxn}}^i \exp\left(-\frac{\Delta G_{\text{b,CO}}^i}{k_B T}\right)}{\sum_i \exp\left(-\frac{\Delta G_{\text{b,CO}}^i}{k_B T}\right)}$$

For the C₁ pathway, *CO hydrogenation to *CHO is more favorable than *CO hydrogenation to *COH, which demands a significantly higher free energy penalty, at both conditions. Specifically, ⟨ΔG_{rxn}⟩ *CHO formation has values of +0.08 eV at LC (-0.6 V_{SHE}) and +0.01 eV at HC (-0.8 V_{SHE}). The corresponding values for *COH formation are +1.68 eV at LC (-0.6 V_{SHE}) and +1.46 eV at HC (-0.8 V_{SHE}) – this stark destabilization of *COH intermediates appears to be due to the linear chain-like nature of the surface B and Cu atoms which do not coordinatively saturate the *COH fragment (Figure 4g), analogous to a “top” site on Cu(111). Indeed, in the case of the most stable *COH binding state in HC (-0.8 V_{SHE}) labelled in Figure 4e, which is also the only *COH state within 0.5 eV of the most stable *CHO state, involves a B chain breakage, creating a “hollow” site in order to coordinatively saturate the *COH fragment (Figure S15) – the energetic cost of B chain breakage, nevertheless, renders the *COH state non-competitive in the electroreduction pathways. Both *CHO and *COH states are significantly destabilized at the Cu sites compared to the B sites. Relative to the lowest energy configuration, the most stable Cu-bound *CHO state is destabilized by +0.94 eV at LC (-0.6 V_{SHE}) and +0.62 eV at - HC (-0.8 V_{SHE}). The corresponding destabilization of the most stable Cu-bound *COH state is 1.51 eV at LC (-0.6 V_{SHE}) and 1.36 eV at HC (-0.8 V_{SHE}). Thus, *CHO formation is more favorable at the more cathodic potential and higher H-coverage and thermodynamically more facile at the B sites than the Cu sites. Sequential hydrogenation from *CO to *CHOH has ⟨ΔG_{rxn}⟩ values of 0.13 eV at LC (-0.6 V_{SHE}) and 0.31 eV at HC (-0.8 V_{SHE}). We calculated free energy barriers for *CHO formation at various sites to estimate the kinetics for entering the C₁ pathway. A spread in *CHO formation barriers is observed and Boltzmann-weighting them by the site-specific ΔG_{b,CO} gives an ensemble-averaged free energy barrier of 0.93 eV at LC (-0.6 V_{SHE}) and 0.78 eV at HC (-0.8 V_{SHE}).

For the C₂ pathway, routes via *CO dimerization, and C–C coupling to form *CO–COH and *CO–CHO were considered. Notably, none of the C–C coupled species were stable on neighboring Cu sites and promptly dissociated upon relaxation. Therefore, we only considered neighboring B sites, and neighboring B and Cu sites, for C₂ pathways. Due to the high destabilization of the initial state containing *COH species relative to *CO and *CHO species, the *CO–COH pathway for the formation of C₂ product is ruled out on all of the considered sites. Both the CO dimerization and the *CO–CHO coupling pathways are probable based on

the free energies of their corresponding intermediates. Specifically, the $\langle \Delta G_{\text{rxn}} \rangle$ for CO dimerization is 0.34 eV at LC (-0.6 V_{SHE}) and 0.15 eV at HC (-0.8 V_{SHE}) when ensemble-averaged across all considered sites. The corresponding value of ΔG_{rxn} on the neighboring Cu–B sites at LC (-0.6 V_{SHE}) (4-8 in Figure 4c) is 0.56 eV, largest among all sites. At HC (-0.8 V_{SHE}), CO dimerization is comparatively more facile at Cu–B site (1-8 in Figure 4f), with a ΔG_{rxn} of 0.26 eV. *CO–CHO formation has a $\langle \Delta G_{\text{rxn}} \rangle$ equal to 0.31 eV and 0.39 eV at LC (-0.6 V_{SHE}) and HC (-0.8 V_{SHE}) respectively. Since *CO–CHO formation through this route must necessarily be preceded by *CHO formation, and the latter's conversion to *CHOH formation is thermodynamically more favorable, we also discard the C–C coupling process for *CO–CHO formation in favor of CO dimerization as an entry point into the C₂ pathway. Free energy barriers for CO dimerization calculated at various sites have an ensemble-average value of 0.55 eV at LC (-0.6 V_{SHE}) and 0.44 eV at HC (-0.8 V_{SHE}).

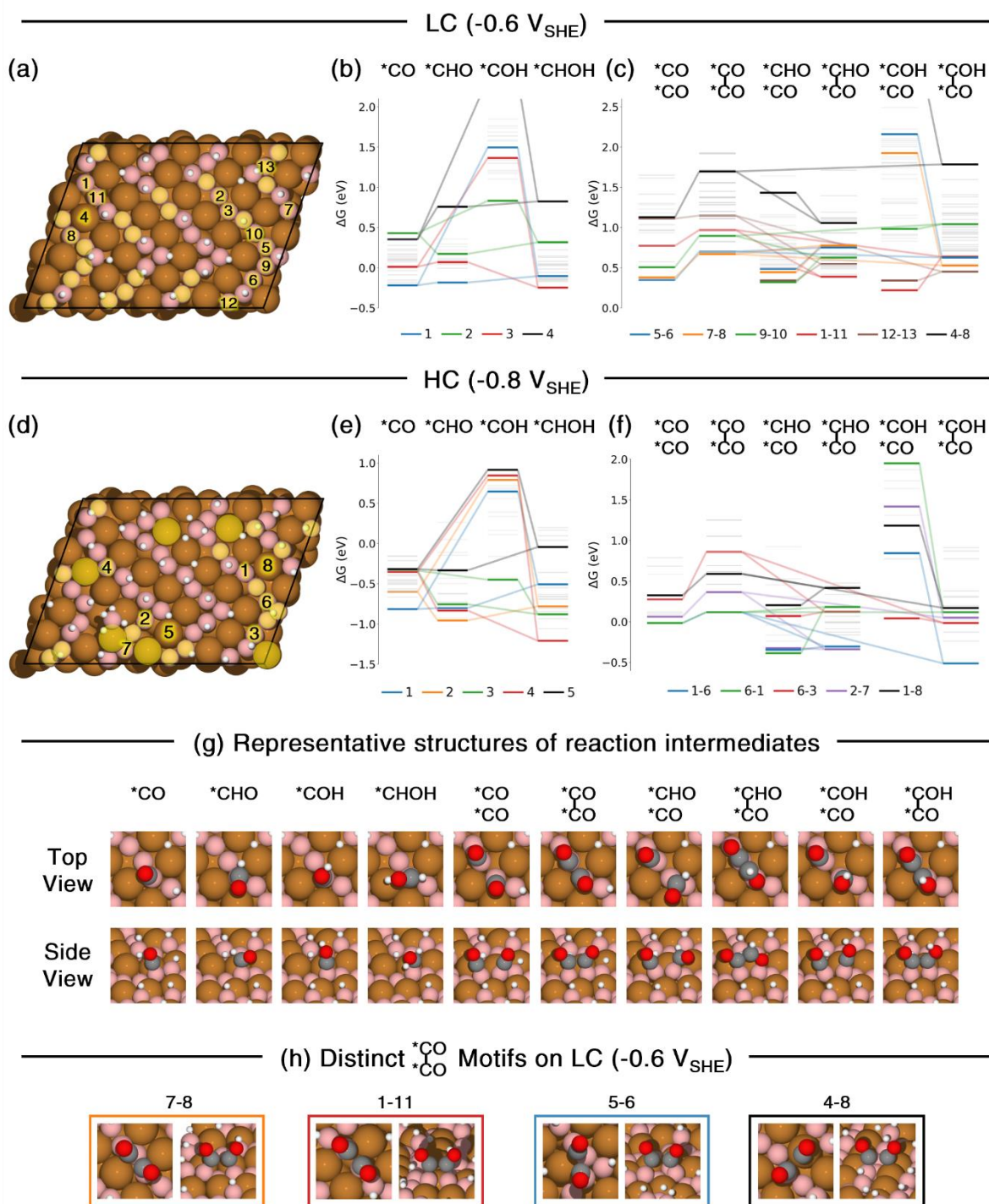


Figure 4. B and Cu sites considered for CORR on predominant H-covered CuB surface configurations (a) LC (-0.6 V_{SHE}) and (d) HC (-0.8 V_{SHE}). Note that the site labels in (a) and (d) correspond to different sites. Gibbs free energy profiles for reaction pathways leading to (b), (e) C_1 and (c,f) C_2 products at LC (-0.6 V_{SHE}) and HC (-0.8 V_{SHE}), respectively. Gibbs free energies are calculated relative to the respective H-covered CuB surface. For each intermediate, the site corresponding to the minimum free energy is highlighted in color and labelled, and all the intermediate states at such sites are connected in the profile. States corresponding to intermediates at all other sites are colored light grey for clarity. (g) CORR

reaction intermediate structures on site 3 at LC (-0.6 V_{SHE}). (h) *C₂O₂ motifs on distinct sites at LC (-0.6 V_{SHE}) including B₃ (7-8, 5-6), B₂ (1-11), and Cu-B (4-8) sites.

The configuration for CO dimerization, involving two *CO molecules on nearby sites, incurs a thermodynamic penalty relative to the one *CO configurations. Thus, it may not be appropriate to compare the intrinsic free energy barriers for the *CHO formation and CO dimerization processes directly, since they are referenced to different initial states. We therefore compare Gibbs free energies of the transition states (ΔG^\ddagger) for CO dimerization and *CHO formation directly and quantify C₂/C₁ selectivity using $\Delta\Delta G^\ddagger$ (CO dimerization – *CHO formation) (Figure 5). As noted previously, we expect the lower H coverage state, represented by the LC (-0.6 V_{SHE}) state, to dominate the catalyst ensemble at operational timescales due to kinetics associated with excess hydrogenation and B chain breaking, even at lower electrode potentials at which HC (-0.8 V_{SHE}) is thermodynamically more stable. We therefore calculate the C₂/C₁ selectivity at the LC (-0.6 V_{SHE}) state (and at the HC (-0.8 V_{SHE}) state, for comparison) as a function of the varying electrode potential. While C₁ and C₂ processes appear evenly matched for the LC (-0.6 V_{SHE}) state of the catalyst near -0.5 V_{SHE}, the calculated C₂:C₁ distribution indicates increasing C₂ selectivity as the electrode potential is further lowered, with complete C₂ selectivity near -1.5 V_{SHE}. This is qualitatively similar to the selectivity switch observed by Sargent et al. in the case of B-doped Cu.²¹ In contrast, the HC (-0.8 V_{SHE}) state of the catalyst shows complete C₁ selectivity across the potential range considered here. Thus, the kinetically metastable LC (-0.6 V_{SHE}) state of the catalyst endows it with high C₂ selectivity at electrode potentials below -0.6 V_{SHE}. Transition to the thermodynamically more stable HC (-0.8 V_{SHE}) would likely abolish C₂ selectivity – unless other C₂ pathways not considered here prevail – and promote C₁ product formation.

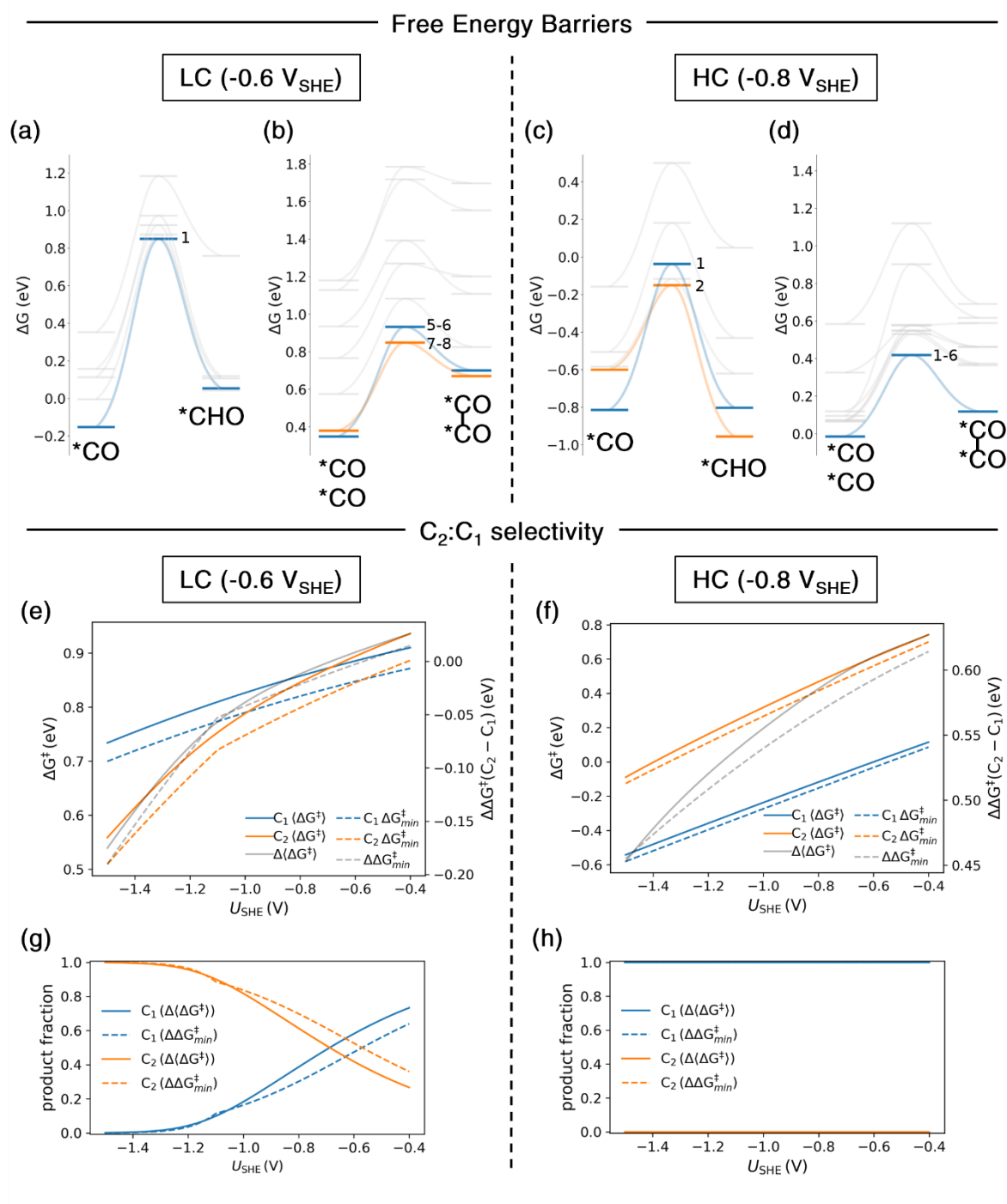


Figure 5. Free energy barriers for (a) *CHO formation and (b) CO dimerization at LC (-0.6 V_{SHE}); (c) *CHO formation and (d) CO dimerization HC (-0.8 V_{SHE}). Only the sites with the lowest energy transition state, initial state, or final state are colored and labeled; the coloring and labeling schemes from corresponding pathways in Figure 4 are maintained here. Minimum and ensemble-averaged ΔG^\ddagger for entering C₁ and C₂ pathways and their difference ($\Delta\Delta G^\ddagger$) at (e) LC (-0.6 V_{SHE}) and (f) HC (-0.8 V_{SHE}) as a function of electrode potential. C₁ and C₂ product distribution calculated for (e) LC (-0.6 V_{SHE}) and (f) HC (-0.8 V_{SHE}) as a function of electrode potential. All Gibbs free energies are calculated relative to the respective H-covered CuB surface.

HER is generally an unavoidable side-reaction in aqueous electrocatalysis,^{6,21,26,27,35} competing with eCO₂RR, particularly when sharing similar onset potentials. We therefore inspected the tendencies of the predominant H-covered CuB surfaces LC (-0.6 V_{SHE}) and HC (-0.8 V_{SHE}) to undergo HER. We considered both the Tafel and Volmer-Heyrovsky mechanisms at these configurations. The Tafel barriers (two *H coupling involving the least strongly bound *H) for the preferred configurations at LC (-0.6 V_{SHE}) (with $n_H = 26$ per unit cell) and HC (-0.8 V_{SHE}) (with $n_H = 39$ per unit cell) were calculated to be 0.52 eV and 0.26 eV respectively. The Volmer-Heyrovsky mechanism involves the initial Volmer step (*H_{*n*} + H⁺ + e⁻ → *H_{*n+1*}) and the subsequent Heyrovsky step (*H_{*n+1*} + H⁺ + e⁻ → *H_{*n*} + H₂) resulting in hydrogen evolution. We calculated the ΔG_{rxn} for each step starting from the aforementioned global minimum configurations with implicit solvation. At LC (-0.6 V_{SHE}), the relevant process was *H₂₆ → *H₂₇ → *H₂₆, where the ΔG_{rxn} for the Volmer and Heyrovsky steps were +0.20 eV and -0.14 eV respectively. At HC (-0.8 V_{SHE}), the relevant process was *H₃₉ → *H₄₀ → *H₃₉, where the Volmer and Heyrovsky steps involved ΔG_{rxn} of +0.26 eV and -0.60 eV respectively. Clearly, in both cases the penalty for HER originates from the initial change in configuration starting from a global minimum structure. Volmer-Heyrovsky steps may also be initiated from closely related structures, which can be accessible during operational conditions while involving the global minimum structure as an intermediate state. At LC (-0.6 V_{SHE}), considering the process originating from a *H₂₅ state (+0.04 eV above the global minimum *H₂₆), *H₂₅ → *H₂₆ → *H₂₅, we find that the Volmer and Heyrovsky steps have ΔG_{rxn} of -0.04 eV and +0.10 eV respectively. The case is slightly different at HC (-0.8 V_{SHE}), where the process originating from a *H₃₈ state (+0.04 eV above the global minimum *H₃₉), *H₃₈ → *H₃₉ → *H₃₈, has both the Volmer and Heyrovsky steps being thermodynamically favorable with ΔG_{rxn} equal to -0.04 eV and -0.29 eV respectively. Other states with potentially more favorable HER thermodynamics may participate in HER but are likely to not be prominent owing to their relatively miniscule populations. In summary, we find HER to be an unavoidable and competing process parallel to CO₂RR, as also observed by Sargent and co-workers in the case of B-doped Cu.²¹ Additionally, persistent HER on the surface likely plays a role in maintaining the intermediate H coverage, preventing the system from reaching very high H coverage, and thereby preserving the B chains on the surface.

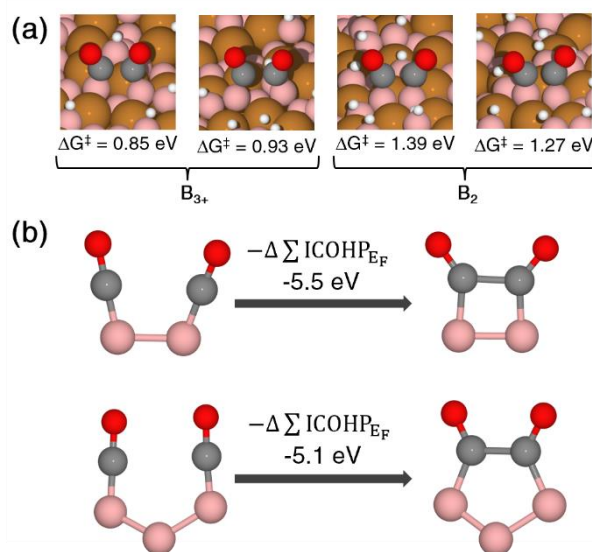


Figure 6. (a) Lowest energy CO dimerization transition states on B₂ and B₃₊ chains and their corresponding Gibbs free energies. (b) B-C-O fragments involved in lowest energy CO dimerization at B₂ (top) and B₃ (bottom) sites and their respective change in $-ICOHP_{E_F}$ values upon dimerization.

A closer look at configurations with most facile CO dimerization (Figure 6a) reveals that each of them involves CO adsorption on alternate B atoms in B₃₊ chains whereas other configurations involve CO adsorption on adjacent B atoms, either in B₂ or B₃₊ chains, prior to coupling. To gain further insight into the higher C₂ activity of configurations with CO adsorbed on alternate sites in B₃₊ chains relative to those adsorbed on B₂ chains, we performed crystal orbital Hamilton population (COHP) analysis³⁸ of the fragments involving the respective B sites and CO molecules in the reactant and product states of CO dimerization. The obtained COHP is integrated up to the Fermi level to yield negative integrated COHP ($-ICOHP_{E_F}$), which acts as a descriptor of the strength of the covalent and noncovalent interactions. In line with the positive ΔG_{rxn} for CO dimerization, a decrease in the magnitude of $-ICOHP_{E_F}$ along the reaction coordinate was observed. It was noted that, for the B₃ site (i.e., three consecutive B atoms on a B₃₊ chain) under consideration, the change of magnitude of $-ICOHP_{E_F}$ was much lower compared to the B₂ sites (i.e., two consecutive B atoms on a B₂ chain) – likely arising from the lower extent of distortion and strain in the fragment upon CO dimerization to form a five-membered ring at a B₃ site versus a four-membered ring at a B₂ site (Figure 6). This provides an indication as to why CO dimerization is easier at the B₃ site.

Conclusion

In summary, we have presented a realistic model of a surface copper boride under operational electrochemical conditions, followed by mechanistic studies of eCORR that indicate C₂ selectivity of this electrocatalyst. Excess B hydrogenation was found to cause B chain breaking, and surface degradation under cathodic potentials. However, this process is kinetically inhibited by HER under operational conditions, resulting in a kinetically metastable H-covered copper boride surface. A potential-dependent grand canonical ensemble for the metastable configurations of the H-covered catalyst surface was constructed using GCGA global optimization and GCDFT calculations. Two configurations of the catalyst, namely, LC (-0.6 V_{SHE}) and HC (-0.8 V_{SHE}) were identified to dominate this ensemble, with the formation of the latter again appearing to be kinetically hindered. Investigation of C₁ and C₂ pathways for eCORR on these configurations revealed site-dependent reactivity with B sites significantly outperforming Cu sites in CO binding and electroreduction. The LC (-0.6 V_{SHE}) configuration is C₂-selective at electrode potentials under -0.6 V_{SHE}, facilitating the C–C coupling (via *CO dimerization) over CO hydrogenation (via *CHO formation). In contrast, the HC (-0.8 V_{SHE}) is C₁-selective under all relevant potentials. Thus, the metastability of the LC (-0.6 V_{SHE}) state of the catalyst endows it with high C₂ selectivity at electrode potentials below -0.6 V_{SHE}. This C₂ selectivity is primarily attributed to neighboring B sites in B₃₊ chains rather than neighboring B sites in B₂ chains, as supported by chemical bonding analysis. Overall, this work highlights the unusual and very important B-centered reactivity on the surface copper boride, demonstrating the potential of leveraging B-centered reactivity on transition metal boride surfaces to drive electrocatalytic processes, including the challenging reduction of CO₍₂₎ to C₂ products.^{39,40}

Computational Methods

Model Setup

We constructed the unit cell with cell dimension of $21.84 \text{ \AA} \times 15.96 \text{ \AA}$ with $\alpha = 70.28^\circ$ (as reported experimentally²³) consisting of a 4×1 supercell of surface copper boride on a 3-layer $\sqrt{73} \times \sqrt{39}$ superstructure of Cu(111), corresponding to a repeating $\text{Cu}_{32}\text{B}_{56}$ surface. The bottom layer of the slab was constrained as the bulk region with everything else allowed to relax. A vacuum of 20 \AA was added in the z-direction to avoid interaction between periodic images.

DFT Calculations

The local optimizations and energy calculation are performed with the RPBE functional⁴¹ and corresponding pseudopotentials in the projector-augmented wave (PAW)⁴² scheme using the VASP program (version 5.4.4).^{43–46} The convergence criteria for electronic and force minimization were set to 10^{-5} eV and 0.10 eV/\AA during the global optimization and 10^{-6} eV and 0.03 eV/\AA for the final refinement. Due to the relatively large system and sampling size, only the Γ k -point was sampled in the reciprocal space of the Brillouin zone throughout, and the cutoff energy for the kinetic energy of the plane-waves was 400 eV . The vibrational contributions to the free energy by the slab atoms are neglected considering their small contribution and high computational cost.⁴⁷ The zero-point energy (ZPE) and thermal contribution terms of the adsorbates are obtained from frequency calculations and evaluated at 298.15 K , with the partial pressure of gaseous species (H_2 and CO) being set to 1 atm (see Supporting Information, Section S7).

The transition states (TS) were located using climbing image nudged elastic band (CI-NEB) method⁴⁸ and each TS geometry was confirmed to have only one imaginary mode. Bader charges were calculated using the Bader Charge Analysis program.⁴⁹ COHP analysis is performed using the LOBSTER program.³⁸ Quantum theory of atoms in molecules analysis is performed using the critic2 program.⁵⁰ Isosurfaces are visualized using the VESTA program.⁵¹

Grand Canonical Genetic Algorithm

The chemical space of CuB surface reconstruction and H coverage was sampled by grand canonical genetic algorithm (GCGA) global optimization using our open-source GOCIA python package.²⁹ The system is treated as a grand canonical ensemble of H adsorbates, and the search target is to minimize the coverage-dependent grand canonical free energy Ω_{ads} :

$$\Omega_{\text{ads}} = U - TS - \mu_{\text{H}}N_{\text{H}} \approx E^{\text{slab}-n_{\text{H}}} - E^{\text{slab}} - n_{\text{H}}\mu_{\text{H}}$$

where $E^{\text{slab}-n_{\text{H}}}$ and E^{slab} are electronic energies of the adsorbate-covered and the bare CuB surface, respectively. The vibrational contributions to the free energy by the slab atoms are neglected considering their small contribution and high computational cost.⁴⁷ The chemical potential of H, μ_{H} was calculated as:

$$\mu_{\text{H}}(\text{pH}, U, T) = \frac{1}{2}E_{\text{H}_2}^{\text{gas}} - \ln(10)k_{\text{B}}T\text{pH} - |e|U_{\text{SHE}} + (ZPE^{\text{gas}} + C_p^{\text{gas}} - TS^{\text{gas}}) - (ZPE^{\text{ads}} + C_p^{\text{ads}} - TS^{\text{ads}})$$

where the pH and U (in SHE scale)-dependent terms are calculated using the computational hydrogen electrode model. The ZPE and thermal contribution terms of the adsorbates are obtained from frequency calculations and evaluated at 298.15 K.

A population size of 25 and a mutation rate of 40% were used for the GCGA sampling. The pool of initial candidates is generated using the box sampling method in GOCIA, which places adsorbates with random positions and orientations into the sampling box. The surface Cu and B surface atoms are perturbed in the initial generation, and their arrangements are allowed to relax as we sample different H coverages and configurations. Any other surface B configurations other than chains turn out to be thermodynamically unfavorable in the mid to low H coverage regime.

Grand Canonical DFT Calculations

Under constant electrochemical potential, the electrode surface represents a grand canonical ensemble of electrons where the number of electrons is varied to adapt to the change in the work function of the surface. The potential-dependent electronic grand canonical free energy of the surface Ω_{el} was approximated by a surface charging model⁵²

$$\Omega_{el}(U) = E(U) - q(U)FU \approx E(U_0) - \frac{1}{2}C(U - U_0)^2$$

which treats the electrochemical interface as an effective capacitor. Here, $E(U)$ is the electronic energy of the surface under a potential U that is calculated by referencing the Fermi level of the system against the vacuum level. $q(U)$ is the surface charge difference referenced against the neutral system and F is the Faraday constant. U_0 stands for the potential of zero charge in vacuum scale and C is the effective capacitance.

The self-consistent implicit solvation model VASPsol⁵³ is used to represent the polarizable electrolyte region. The surface slab is symmetrized via a point center symmetry operation to avoid an asymmetric potential in the implicit solvation region. The thickness of the implicit solvent slab is increased to 5λ , where λ (the Debye screening length) is evaluated by⁵⁴

$$\lambda \approx \frac{3}{\sqrt{I}} \text{Å}$$

where I is the ionic strength in M; in this study, we take it to be 0.1 to model the 0.1 M KCl electrolyte used by Sargent et al.²¹ Hence, the implicit solvent thickness is set to 50 Å for the symmetrized slab.

By varying the number of electrons in the system, $E(U)$ of the system at the corresponding U and $q(U)$ can be obtained, and thereby, a quadratic relation between $\Omega_{el}(U)$ and U can be fitted by sampling a series of q values. Multiple calculations were performed at extra charges of -3, -2, -1, 0, +1, +2 |e| per simulation box to fit the quadratic potential-dependent free energy relation. The U (in vacuum scale) can be converted into the SHE scale by referencing it against the benchmarked value (4.60 V for VASPsol).⁵⁵

The final coverage- and potential-dependent grand canonical free energy Ω_{tot} was approximated by:

$$\Omega_{tot}(n_H, U) = \Omega_{ads}^{slab-n_H}(U) - \Omega_{ads}^{slab}(U) - n_H\mu_H(\text{pH}, U, T)$$

Given the considerable computational cost involved, the GCDFT calculations were performed not during the GCGA sampling but on a subset of structures (within 0.2 eV from the GM of each coverage state in the metastable plateau) from the final ensemble, *a posteriori*. This approach greatly reduced the computational expense of constructing the potential-dependent grand canonical ensemble while capturing the energetics of key accessible states in the ensemble.

Acknowledgements

This work was supported as part of the Center for Closing the Carbon Cycle, an Energy Frontier Research Center funded by the U.S. Department of Energy, Office of Science, Basic Energy Sciences under Award Number DE-SC0023427. Z. Z. was supported previously by the Dissertation Year Award at UCLA and currently by the Stanford Energy Fellowship at the Stanford Precourt Institute for Energy. Our calculations utilized resources of Perlmutter of the National Energy Research Scientific Computing Center (NERSC) under Contract DE-AC02-05CH11231. We thank Dr. Yulan Han for helpful discussions.

References

- (1) Seh, Z. W.; Kibsgaard, J.; Dickens, C. F.; Chorkendorff, I.; Nørskov, J. K.; Jaramillo, T. F. Combining Theory and Experiment in Electrocatalysis: Insights into Materials Design. *Science* **2017**, *355* (6321), eaad4998. <https://doi.org/10.1126/science.aad4998>.
- (2) *Advances and challenges in understanding the electrocatalytic conversion of carbon dioxide to fuels* | *Nature Energy*. <https://www.nature.com/articles/s41560-019-0450-y> (accessed 2025-03-05).
- (3) Gao, D.; Arán-Ais, R. M.; Jeon, H. S.; Roldan Cuenya, B. Rational Catalyst and Electrolyte Design for CO₂ Electroreduction towards Multicarbon Products. *Nat Catal* **2019**, *2* (3), 198–210. <https://doi.org/10.1038/s41929-019-0235-5>.
- (4) Cabana, J.; Alaan, T.; Crabtree, G. W.; Hatzell, M. C.; Manthiram, K.; Steingart, D. A.; Zenyuk, I.; Jiao, F.; Vojvodic, A.; Yang, J. Y.; Balsara, N. P.; Persson, K. A.; Siegel, D. J.; Haynes, C. L.; Mauzeroll, J.; Shen, M.; Venton, B. J.; Balke, N.; Rodríguez-López, J.; Rolison, D. R.; Shahbazian-Yassar, R.; Srinivasan, V.; Chaudhuri, S.; Couet, A.; Hattrick-Simpers, J. NGenE 2021: Electrochemistry Is Everywhere. *ACS Energy Lett.* **2022**, *7* (1), 368–374. <https://doi.org/10.1021/acscenergylett.1c02608>.
- (5) Wang, L.; Nitopi, S. A.; Bertheussen, E.; Orazov, M.; Morales-Guio, C. G.; Liu, X.; Higgins, D. C.; Chan, K.; Nørskov, J. K.; Hahn, C.; Jaramillo, T. F. Electrochemical Carbon Monoxide Reduction on Polycrystalline Copper: Effects of Potential, Pressure, and pH on Selectivity toward Multicarbon and Oxygenated Products. *ACS Catal.* **2018**, *8* (8), 7445–7454. <https://doi.org/10.1021/acscatal.8b01200>.
- (6) Zhang, G.; Zhao, Z.-J.; Cheng, D.; Li, H.; Yu, J.; Wang, Q.; Gao, H.; Guo, J.; Wang, H.; Ozin, G. A.; Wang, T.; Gong, J. Efficient CO₂ Electroreduction on Facet-Selective Copper Films with

High Conversion Rate. *Nat Commun* **2021**, 12 (1), 5745. <https://doi.org/10.1038/s41467-021-26053-w>.

(7) *Progress and Perspectives of Electrochemical CO₂ Reduction on Copper in Aqueous Electrolyte* | *Chemical Reviews*. <https://pubs.acs.org/doi/10.1021/acs.chemrev.8b00705> (accessed 2025-03-05).

(8) Dattila, F.; Seemakurthi, R. R.; Zhou, Y.; López, N. Modeling Operando Electrochemical CO₂ Reduction. *Chem. Rev.* **2022**, 122 (12), 11085–11130. <https://doi.org/10.1021/acs.chemrev.1c00690>.

(9) Li, J.; Ozden, A.; Wan, M.; Hu, Y.; Li, F.; Wang, Y.; Zamani, R. R.; Ren, D.; Wang, Z.; Xu, Y.; Nam, D.-H.; Wicks, J.; Chen, B.; Wang, X.; Luo, M.; Graetzel, M.; Che, F.; Sargent, E. H.; Sinton, D. Silica-Copper Catalyst Interfaces Enable Carbon-Carbon Coupling towards Ethylene Electrosynthesis. *Nat Commun* **2021**, 12 (1), 2808. <https://doi.org/10.1038/s41467-021-23023-0>.

(10) Xu, A.; Hung, S.-F.; Cao, A.; Wang, Z.; Karmodak, N.; Huang, J. E.; Yan, Y.; Sedighian Rasouli, A.; Ozden, A.; Wu, F.-Y.; Lin, Z.-Y.; Tsai, H.-J.; Lee, T.-J.; Li, F.; Luo, M.; Wang, Y.; Wang, X.; Abed, J.; Wang, Z.; Nam, D.-H.; Li, Y. C.; Ip, A. H.; Sinton, D.; Dong, C.; Sargent, E. H. Copper/Alkaline Earth Metal Oxide Interfaces for Electrochemical CO₂-to-Alcohol Conversion by Selective Hydrogenation. *Nat Catal* **2022**, 5 (12), 1081–1088. <https://doi.org/10.1038/s41929-022-00880-6>.

(11) Li, F.; Thevenon, A.; Rosas-Hernández, A.; Wang, Z.; Li, Y.; Gabardo, C. M.; Ozden, A.; Dinh, C. T.; Li, J.; Wang, Y.; Edwards, J. P.; Xu, Y.; McCallum, C.; Tao, L.; Liang, Z.-Q.; Luo, M.; Wang, X.; Li, H.; O'Brien, C. P.; Tan, C.-S.; Nam, D.-H.; Quintero-Bermudez, R.; Zhuang, T.-T.; Li, Y. C.; Han, Z.; Britt, R. D.; Sinton, D.; Agapie, T.; Peters, J. C.; Sargent, E. H. Molecular Tuning of CO₂-to-Ethylene Conversion. *Nature* **2020**, 577 (7791), 509–513. <https://doi.org/10.1038/s41586-019-1782-2>.

(12) Li, J.; Li, F.; Liu, C.; Wei, F.; Gong, J.; Li, W.; Xue, L.; Yin, J.; Xiao, L.; Wang, G.; Lu, J.; Zhuang, L. Polyquinone Modification Promotes CO₂ Activation and Conversion to C₂+ Products over Copper Electrode. *ACS Energy Lett.* **2022**, 7 (11), 4045–4051. <https://doi.org/10.1021/acsenerylett.2c01955>.

(13) Xiao, H.; Goddard, W. A.; Cheng, T.; Liu, Y. Cu Metal Embedded in Oxidized Matrix Catalyst to Promote CO₂ Activation and CO Dimerization for Electrochemical Reduction of CO₂. *Proc. Natl. Acad. Sci. U.S.A.* **2017**, 114 (26), 6685–6688. <https://doi.org/10.1073/pnas.1702405114>.

(14) De Luna, P.; Quintero-Bermudez, R.; Dinh, C.-T.; Ross, M. B.; Bushuyev, O. S.; Todorović, P.; Regier, T.; Kelley, S. O.; Yang, P.; Sargent, E. H. Catalyst Electro-Redeposition Controls Morphology and Oxidation State for Selective Carbon Dioxide Reduction. *Nat Catal* **2018**, 1 (2), 103–110. <https://doi.org/10.1038/s41929-017-0018-9>.

(15) Ren, D.; Deng, Y.; Handoko, A. D.; Chen, C. S.; Malkhandi, S.; Yeo, B. S. Selective Electrochemical Reduction of Carbon Dioxide to Ethylene and Ethanol on Copper(I) Oxide Catalysts. *ACS Catal.* **2015**, 5 (5), 2814–2821. <https://doi.org/10.1021/cs502128q>.

(16) *Solvothermally-Prepared Cu₂O Electrocatalysts for CO₂ Reduction with Tunable Selectivity by the Introduction of p-Block Elements - Larrazábal - 2017 - ChemSusChem - Wiley*

Online Library. https://chemistry-europe.onlinelibrary.wiley.com/doi/full/10.1002/cssc.201601578 (accessed 2025-03-05).

(17) Lee, S.; Kim, D.; Lee, J. Electrocatalytic Production of C3-C4 Compounds by Conversion of CO₂ on a Chloride-Induced Bi-Phasic Cu₂O-Cu Catalyst. *Angewandte Chemie International Edition* **2015**, *54* (49), 14701–14705. <https://doi.org/10.1002/anie.201505730>.

(18) Favaro, M.; Xiao, H.; Cheng, T.; Goddard, W. A.; Yano, J.; Crumlin, E. J. Subsurface Oxide Plays a Critical Role in CO₂ Activation by Cu(111) Surfaces to Form Chemisorbed CO₂, the First Step in Reduction of CO₂. *Proceedings of the National Academy of Sciences* **2017**, *114* (26), 6706–6711. <https://doi.org/10.1073/pnas.1701405114>.

(19) Li, M.; Ma, Y.; Chen, J.; Lawrence, R.; Luo, W.; Sacchi, M.; Jiang, W.; Yang, J. Residual Chlorine Induced Cationic Active Species on a Porous Copper Electrocatalyst for Highly Stable Electrochemical CO₂ Reduction to C₂+. *Angewandte Chemie International Edition* **2021**, *60* (20), 11487–11493. <https://doi.org/10.1002/anie.202102606>.

(20) Lim, H.-K.; Shin, H.; Goddard, W. A. I.; Hwang, Y. J.; Min, B. K.; Kim, H. Embedding Covalency into Metal Catalysts for Efficient Electrochemical Conversion of CO₂. *J. Am. Chem. Soc.* **2014**, *136* (32), 11355–11361. <https://doi.org/10.1021/ja503782w>.

(21) Zhou, Y.; Che, F.; Liu, M.; Zou, C.; Liang, Z.; De Luna, P.; Yuan, H.; Li, J.; Wang, Z.; Xie, H.; Li, H.; Chen, P.; Bladt, E.; Quintero-Bermudez, R.; Sham, T.-K.; Bals, S.; Hofkens, J.; Sinton, D.; Chen, G.; Sargent, E. H. Dopant-Induced Electron Localization Drives CO₂ Reduction to C₂ Hydrocarbons. *Nature Chem* **2018**, *10* (9), 974–980. <https://doi.org/10.1038/s41557-018-0092-x>.

(22) Wang, S.; Wang, L.; Zhu, X.; Zhuang, Y.; Niu, X.; Zhao, Q. A Covalency-Aided Electrochemical Mechanism for CO₂ Reduction: The Synergistic Effect of Copper and Boron Dual Active Sites Drives the Formation of a High-Efficiency Ethanol Product. *Nanoscale* **2023**, *15* (44), 17776–17784. <https://doi.org/10.1039/D3NR04288J>.

(23) Yue, C.; Weng, X.-J.; Gao, G.; Oganov, A. R.; Dong, X.; Shao, X.; Wang, X.; Sun, J.; Xu, B.; Wang, H.-T.; Zhou, X.-F.; Tian, Y. Formation of Copper Boride on Cu(111). *Fundamental Research* **2021**, *1* (4), 482–487. <https://doi.org/10.1016/j.fmre.2021.05.003>.

(24) Weng, X.-J.; Bai, J.; Hou, J.; Zhu, Y.; Wang, L.; Li, P.; Nie, A.; Xu, B.; Zhou, X.-F.; Tian, Y. Experimental Evidence of Surface Copper Boride. *Nano Res.* **2023**, *16* (7), 9602–9607. <https://doi.org/10.1007/s12274-023-5496-2>.

(25) Tsujikawa, Y.; Zhang, X.; Horio, M.; Komori, F.; Nakashima, T.; Ando, Y.; Kondo, T.; Matsuda, I. Structure and Electronic State of Boron Atomic Chains on a Noble Metal (111) Surface. *e-J. Surf. Sci. Nanotechnol.* **2023**, *22* (1), 1–8. <https://doi.org/10.1380/ejsnt.2023-058>.

(26) Zhang, Z.; Wei, Z.; Sautet, P.; Alexandrova, A. N. Hydrogen-Induced Restructuring of a Cu(100) Electrode in Electroreduction Conditions. *J. Am. Chem. Soc.* **2022**, *144* (42), 19284–19293. <https://doi.org/10.1021/jacs.2c06188>.

(27) Cheng, D.; Wei, Z.; Zhang, Z.; Broekmann, P.; Alexandrova, A. N.; Sautet, P. Restructuring and Activation of Cu(111) under Electrocatalytic Reduction Conditions. *Angewandte Chemie* **2023**, *135* (20), e202218575. <https://doi.org/10.1002/ange.202218575>.

- (28) Zhang, Z.; Gee, W.; Sautet, P.; Alexandrova, A. N. H and CO Co-Induced Roughening of Cu Surface in CO₂ Electroreduction Conditions. *J. Am. Chem. Soc.* **2024**, *146* (23), 16119–16127. <https://doi.org/10.1021/jacs.4c03515>.
- (29) Zhang, Z.; Gee, W.; Lavroff, R. H.; Alexandrova, A. N. GOCIA: A Grand Canonical Global Optimizer for Clusters, Interfaces, and Adsorbates. *Phys. Chem. Chem. Phys.* **2025**, *27* (2), 696–706. <https://doi.org/10.1039/D4CP03801K>.
- (30) Bader, R. F. W. *Atoms in Molecules: A Quantum Theory*; Oxford University Press Oxford, 1990. <https://doi.org/10.1093/oso/9780198551683.001.0001>.
- (31) Bader, R. F. W. A Quantum Theory of Molecular Structure and Its Applications. *Chem. Rev.* **1991**, *91* (5), 893–928. <https://doi.org/10.1021/cr00005a013>.
- (32) Poths, P.; Vargas, S.; Sautet, P.; Alexandrova, A. N. Thermodynamic Equilibrium versus Kinetic Trapping: Thermalization of Cluster Catalyst Ensembles Can Extend Beyond Reaction Time Scales. *ACS Catal.* **2024**, *14* (7), 5403–5415. <https://doi.org/10.1021/acscatal.3c06154>.
- (33) Montoya, J. H.; Shi, C.; Chan, K.; Nørskov, J. K. Theoretical Insights into a CO Dimerization Mechanism in CO₂ Electroreduction. *J. Phys. Chem. Lett.* **2015**, *6* (11), 2032–2037. <https://doi.org/10.1021/acs.jpcllett.5b00722>.
- (34) Xiao, H.; Cheng, T.; Goddard, W. A.; Sundararaman, R. Mechanistic Explanation of the pH Dependence and Onset Potentials for Hydrocarbon Products from Electrochemical Reduction of CO on Cu (111). *J. Am. Chem. Soc.* **2016**, *138* (2), 483–486. <https://doi.org/10.1021/jacs.5b11390>.
- (35) Cheng, T.; Xiao, H.; Goddard, W. A. Full Atomistic Reaction Mechanism with Kinetics for CO Reduction on Cu(100) from Ab Initio Molecular Dynamics Free-Energy Calculations at 298 K. *Proc. Natl. Acad. Sci. U.S.A.* **2017**, *114* (8), 1795–1800. <https://doi.org/10.1073/pnas.1612106114>.
- (36) Garza, A. J.; Bell, A. T.; Head-Gordon, M. Mechanism of CO₂ Reduction at Copper Surfaces: Pathways to C₂ Products. *ACS Catal.* **2018**, *8* (2), 1490–1499. <https://doi.org/10.1021/acscatal.7b03477>.
- (37) Todorova, T. K.; Schreiber, M. W.; Fontecave, M. Mechanistic Understanding of CO₂ Reduction Reaction (CO₂RR) Toward Multicarbon Products by Heterogeneous Copper-Based Catalysts. *ACS Catal.* **2020**, *10* (3), 1754–1768. <https://doi.org/10.1021/acscatal.9b04746>.
- (38) *LOBSTER: Local orbital projections, atomic charges, and chemical-bonding analysis from projector-augmented-wave-based density-functional theory - Nelson - 2020 - Journal of Computational Chemistry - Wiley Online Library.* <https://onlinelibrary.wiley.com/doi/full/10.1002/jcc.26353> (accessed 2025-03-05).
- (39) Zhu, C.; Wen, C.; Wang, M.; Zhang, M.; Geng, Y.; Su, Z. Non-Metal Boron Atoms on a CuB₁₂ Monolayer as Efficient Catalytic Sites for Urea Production. *Chem. Sci.* **2022**, *13* (5), 1342–1354. <https://doi.org/10.1039/D1SC04845G>.
- (40) Liu, M.; Balamurugan, J.; Liang, T.; Liu, C. Theoretical Study of B₁₂ Borophene Supported Metal for Electrocatalytic CO₂ Reduction Reaction. *Applied Surface Science* **2024**, *642*, 158594. <https://doi.org/10.1016/j.apsusc.2023.158594>.

- (41) Hammer, B.; Hansen, L. B.; Nørskov, J. K. Improved Adsorption Energetics within Density-Functional Theory Using Revised Perdew-Burke-Ernzerhof Functionals. *Phys. Rev. B* **1999**, *59* (11), 7413–7421. <https://doi.org/10.1103/PhysRevB.59.7413>.
- (42) Kresse, G.; Joubert, D. From Ultrasoft Pseudopotentials to the Projector Augmented-Wave Method. *Phys. Rev. B* **1999**, *59* (3), 1758–1775. <https://doi.org/10.1103/PhysRevB.59.1758>.
- (43) Kresse, G.; Furthmüller, J. Efficiency of Ab-Initio Total Energy Calculations for Metals and Semiconductors Using a Plane-Wave Basis Set. *Computational Materials Science* **1996**, *6* (1), 15–50. [https://doi.org/10.1016/0927-0256\(96\)00008-0](https://doi.org/10.1016/0927-0256(96)00008-0).
- (44) Kresse, G.; Furthmüller, J. Efficient Iterative Schemes for *Ab Initio* Total-Energy Calculations Using a Plane-Wave Basis Set. *Phys. Rev. B* **1996**, *54* (16), 11169–11186. <https://doi.org/10.1103/PhysRevB.54.11169>.
- (45) Kresse, G. Ab Initio Molecular Dynamics for Liquid Metals. *Journal of Non-Crystalline Solids* **1995**, *192–193*, 222–229. [https://doi.org/10.1016/0022-3093\(95\)00355-X](https://doi.org/10.1016/0022-3093(95)00355-X).
- (46) Kresse, G.; Hafner, J. *Ab Initio* Molecular-Dynamics Simulation of the Liquid-Metal–Amorphous-Semiconductor Transition in Germanium. *Phys. Rev. B* **1994**, *49* (20), 14251–14269. <https://doi.org/10.1103/PhysRevB.49.14251>.
- (47) Sun, G.; Alexandrova, A. N.; Sautet, P. Structural Rearrangements of Subnanometer Cu Oxide Clusters Govern Catalytic Oxidation. *ACS Catal.* **2020**, *10* (9), 5309–5317. <https://doi.org/10.1021/acscatal.0c00824>.
- (48) Henkelman, G.; Uberuaga, B. P.; Jónsson, H. A Climbing Image Nudged Elastic Band Method for Finding Saddle Points and Minimum Energy Paths. *The Journal of Chemical Physics* **2000**, *113* (22), 9901–9904. <https://doi.org/10.1063/1.1329672>.
- (49) Yu, M.; Trinkle, D. R. Accurate and Efficient Algorithm for Bader Charge Integration. *The Journal of Chemical Physics* **2011**, *134* (6), 064111. <https://doi.org/10.1063/1.3553716>.
- (50) Otero-de-la-Roza, A.; Johnson, E. R.; Luaña, V. Critic2: A Program for Real-Space Analysis of Quantum Chemical Interactions in Solids. *Computer Physics Communications* **2014**, *185* (3), 1007–1018. <https://doi.org/10.1016/j.cpc.2013.10.026>.
- (51) Momma, K.; Izumi, F. VESTA 3 for Three-Dimensional Visualization of Crystal, Volumetric and Morphology Data. *J Appl Crystallogr* **2011**, *44* (6), 1272–1276. <https://doi.org/10.1107/S0021889811038970>.
- (52) Steinmann, S. N.; Michel, C.; Schwiedernoch, R.; Sautet, P. Impacts of Electrode Potentials and Solvents on the Electroreduction of CO₂: A Comparison of Theoretical Approaches. *Phys. Chem. Chem. Phys.* **2015**, *17* (21), 13949–13963. <https://doi.org/10.1039/C5CP00946D>.
- (53) Mathew, K.; Sundararaman, R.; Letchworth-Weaver, K.; Arias, T. A.; Hennig, R. G. Implicit Solvation Model for Density-Functional Study of Nanocrystal Surfaces and Reaction Pathways. *The Journal of Chemical Physics* **2014**, *140* (8), 084106. <https://doi.org/10.1063/1.4865107>.
- (54) Steinmann, S. N.; Sautet, P. Assessing a First-Principles Model of an Electrochemical Interface by Comparison with Experiment. *J. Phys. Chem. C* **2016**, *120* (10), 5619–5623. <https://doi.org/10.1021/acs.jpcc.6b01938>.

(55) Mathew, K.; Kolluru, V. S. C.; Mula, S.; Steinmann, S. N.; Hennig, R. G. Implicit Self-Consistent Electrolyte Model in Plane-Wave Density-Functional Theory. *The Journal of Chemical Physics* **2019**, *151* (23), 234101. <https://doi.org/10.1063/1.5132354>.

TOC Graphic

